The Astrophysical Journal, 775:86 (14pp), 2013 October 1 doi:10.1088/0004-637X/775/2/86

SOLAR RADIATION PRESSURE AND LOCAL INTERSTELLAR MEDIUM FLOW PARAMETERS FROM *INTERSTELLAR BOUNDARY EXPLORER* LOW ENERGY HYDROGEN MEASUREMENTS

N. A. Schwadron[1,8], E. Moebius[1], H. Kucharek[1], M. A. Lee[1], J. French[1], L. Saul[2], P. Wurz[2], M. Bzowski[3], S. A. Fuselier[4], G. Livadiotis[4], D. J. McComas[4,9], P. Frisch[5], M. Gruntman[6], and H. R. Mueller[7]
[1] University of New Hampshire, Durham, NH 03824, USA
[2] University of Bern, 3012 Bern, Switzerland
[3] Space Research Centre of the Polish Academy of Sciences, Warsaw, Poland
[4] Southwest Research Institute, San Antonio, TX 78228, USA
[5] University of Chicago, Chicago, IL 60637, USA
[6] University of Southern California, Los Angeles, CA 90089, USA
[7] Dartmouth College, Hanover, NH 03755, USA
Received 2013 March 30; accepted 2013 July 27; published 2013 September 9

ABSTRACT

Neutral hydrogen atoms that travel into the heliosphere from the local interstellar medium (LISM) experience strong effects due to charge exchange and radiation pressure from resonant absorption and re-emission of Lyα. The radiation pressure roughly compensates for the solar gravity. As a result, interstellar hydrogen atoms move along trajectories that are quite different than those of heavier interstellar species such as helium and oxygen, which experience relatively weak radiation pressure. Charge exchange leads to the loss of primary neutrals from the LISM and the addition of new secondary neutrals from the heliosheath. *IBEX* observations show clear effects of radiation pressure in a large longitudinal shift in the peak of interstellar hydrogen compared with that of interstellar helium. Here, we compare results from the Lee et al. interstellar neutral model with *IBEX*-Lo hydrogen observations to describe the distribution of hydrogen near 1 AU and provide new estimates of the solar radiation pressure. We find over the period analyzed from 2009 to 2011 that radiation pressure divided by the gravitational force (μ) has increased slightly from $\mu = 0.94 \pm 0.04$ in 2009 to $\mu = 1.01 \pm 0.05$ in 2011. We have also derived the speed, temperature, source longitude, and latitude of the neutral H atoms and find that these parameters are roughly consistent with those of interstellar He, particularly when considering the filtration effects that act on H in the outer heliosheath. Thus, our analysis shows that over the period from 2009 to 2011, we observe signatures of neutral H consistent with the primary distribution of atoms from the LISM and a radiation pressure that increases in the early rise of solar activity.

Key words: ISM: abundances – ISM: atoms – solar wind – Sun: heliosphere

Online-only material: color figures

1. INTRODUCTION

As the Sun moves through the local galactic medium, its supersonic, ionized solar wind carves out the heliosphere. The motion of the heliosphere through the Galactic medium provides a relative velocity between the local interstellar medium (LISM) and the heliosphere. Ions in the LISM are deflected by and flow around the heliosphere, whereas neutral atoms are free to travel relatively unperturbed through the heliosphere and can be detected by the *Interstellar Boundary Explorer* (*IBEX*)-Lo sensor.

Recent observations from *IBEX*-Lo (Möbius et al. 2012; Bzowski et al. 2012; McComas et al. 2012; McComas 2012) show that the motion of the Sun relative to the surrounding medium is slower and in a somewhat different direction than previously thought (Möbius et al. 2004; Witte et al. 2004, 1993). Consensus values based on He measurements from *IBEX*-Lo provide a LISM speed of 23.2 ± 0.3 km s^{-1} and a flow direction of ($79.^\circ00 \pm 0.^\circ47$, $-4.^\circ98 \pm 0.^\circ21$) in ecliptic longitude and latitude and an interstellar He temperature of 6300 ± 390 K (McComas 2012). This flow direction implies a nose direction for the heliosphere of $\sim$($259.^\circ00$, $4.^\circ98$). The He measurements are considered excellent indicators of interstellar conditions since He, due to its high ionization potential, interacts only weakly with the heliosheath and outflowing solar wind.

Measurements of H have also been reported. A well-known study by Lallement et al. (2005), recently updated (Lallement et al. 2010), based on Lyα resonant absorption and re-emission by inflowing interstellar neutral (ISN) H atoms finds a speed of 22 ± 1 km s^{-1}, a temperature of $11{,}500 \pm 1000$ K, and a flow direction of ($72.^\circ5 \pm 0.^\circ7$, $-8.^\circ9 \pm 0.^\circ5$) in ecliptic longitude and latitude. The slowing, deflection, and effective heating of the H neutrals is due to the existence of a "secondary" neutral population generated from charge exchange with the slowed and heated plasma in the outer heliosheath (Wallis 1975; Holzer 1977; Baranov & Malama 1993). The secondary neutral population is seen as an absorption component in high-resolution *Hubble Space Telescope* spectra of stellar Lyα profiles of nearby stars (Linsky & Wood 1996; Wood et al. 2007a, 2007b).

The "primary" population of H is composed of original atoms from the LISM that travel through the heliosheath and into the inner heliosphere. The charge-exchange interactions of H in the outer heliosheath represent a loss (or "filtration") process for the primary H population, which has been quantified (see Bzowski et al. 2011 and references therein). Filtration acts preferentially on slower H atoms, causing a $\sim$2 km s^{-1} average increase of the primary flow speed and a $\sim$400 K reduction in the effective temperature of the distribution.

[8] Also at Southwest Research Institute, San Antonio, TX 78228, USA.
[9] Also at University of Texas, San Antonio, TX 78228, USA.

Recently, Saul et al. (2012) used *IBEX*-Lo observations to observe low energy LISM H atoms within the heliosphere. The observations were found to be consistent with ISN H experiencing an effective ratio of outward solar radiation pressure to inward gravitational force greater than unity ($\mu > 1$). The temporal change observed in the ISN H flux was explained based on increasing solar activity, which presumably caused the solar Lyα intensity and therefore the solar radiation pressure to increase with time.

This paper extends the observational analysis of Saul et al. (2012) by comparing observations with an analytical model of interstellar atoms entering the heliosphere (Lee et al. 2012). This analytical model takes into account ionization processes (photoionization and charge exchange), solar gravity, and radiation pressure to solve for the distribution function of LISM atoms observed by *IBEX*. The model of Lee et al. (2012) only applies inside the termination shock. Therefore, we are restricted here to solving for the distribution of hydrogen atoms that enter through the termination shock and we cannot directly infer the properties of H atoms from the pristine LISM far beyond the heliosphere. As outlined previously, the effects of charge exchange within the heliosheath lead to filtration of the primary component and the generation of a secondary component of the incident neutral population. We will show that signatures consistent with both filtration of the primary component and the secondary component are observed in the neutral H distributions observed by *IBEX*-Lo.

2. DISTRIBUTIONS OBSERVED BY *IBEX*-Lo

IBEX has two energetic neutral atom (ENA) sensors for heliospheric remote sensing and measurements of interstellar neutral atoms (McComas et al. 2009). The *IBEX*-Lo sensor measures ENAs and interstellar neutral atoms from ~10 eV to 2 keV and includes time-of-flight analysis to provide compositional information of interstellar atoms (Fuselier et al. 2009). The *IBEX-Hi* sensor measures ENAs from ~300 eV to 6 keV (Funsten et al. 2009).

The *IBEX*-Lo entrance system accepts incoming neutral atoms through a large-area collimator with a 7° full width at half Maximum (FWHM). After passing through the collimator, neutrals reach a conversion surface where a small fraction are converted into negative ions and are then filtered based on their energy and charge by an electrostatic analyzer. Post acceleration, negative ions pass through a time-of-flight system, which, together with the energy and charge measurements, determines the mass and therefore the atomic species of these ions.

The effect of the conversion surface is different for H and He. Incoming H atoms are predominantly converted into H^-, whereas He atoms predominantly sputter H^- ions. During optimal LISM He observing periods in the spring of each year, the motion of *IBEX*, which moves with Earth around the Sun at ~30 km s^{-1}, opposes the velocity of incident neutral atoms.

LISM He atoms, based on *IBEX*-Lo observations, move at an average speed of ~23.2 km s^{-1} relative to the Sun in the outer heliosphere. *Ulysses* results indicate a faster ~26 km s^{-1} inflow speed of He neutrals. The He atoms that have an average speed of 23.2 km s^{-1} at the termination shock and make it in to 1 AU increase their energy and speed to ~48 km s^{-1} due to the Sun's gravitational attraction. During the *IBEX*-Lo He observing periods, incident ISN He atoms have typical speeds of ~78 km s^{-1} into the *IBEX*-Lo sensor, which implies a kinetic energy of ~130 eV that is similar to the 110 eV central acceptance energy of step 4 of the *IBEX*-Lo electrostatic analyzer (ESA). While the LISM He temperature slightly broadens the distribution, the incoming ISN He distribution is remarkably narrow and beam-like. The *IBEX*-Lo ESA steps admit a broad range of energies ($\Delta E/E \sim 0.7$), from which it follows that the vast majority of these He atoms fall within ESA step 4. Sputtered products of the incident He atoms have energies less than the parent atom. Therefore, the sputtered H^- ions are observed in ESA steps 1–4. The peak sputtering response from incident atoms from ESA 4 for sputtering occurs in ESA 3. Therefore, in the *IBEX* orbits where the *IBEX*-Lo sensor is oriented to allow large fluxes of ISN He atoms into the collimator, we observe the largest count rate in ESA 3 and smaller, but still sizable count rates, in ESA 2, ESA 1, and ESA 4. This important signature provides a straightforward identification of ISN He in *IBEX* observations.

ISN H atoms, in contrast to the sputtering by He, are directly converted into H^- on the conversion surface. As a result, we observe the largest count rates for ISN H at the ESA step with a central energy closest to the kinetic energy of the incident H atoms. ISN H atoms experience a strong outward radiation pressure due to resonant absorption and re-emission of Lyα. The radiation pressure roughly compensates for the gravitational attraction, which implies that H atoms from the LISM have a speed of ~20–30 km s^{-1} at 1 AU when they are observed by *IBEX*. Taking into account the ~30 km s^{-1} relative motion of *IBEX* with respect to the Sun, we find that incident LISM H atoms have energies of ~13–19 eV, which falls in the energy range of ESA 1 (the central energy of ESA 1 is 15 eV). The signature of LISM H atoms provides a large count rate in ESA 1.

The signatures of H and He are shown clearly in Figure 1. In particular, note that the H distribution at ESA 1 shown in the top panel has a much larger longitudinal distribution than the distribution in ESA 3 due to LISM He. The broader longitudinal distribution can be ascribed to several factors. Most importantly, the fact that H has a smaller mass than He implies that the thermal speed of H atoms should be about twice that of He if there is a common LISM temperature of H and He. The larger thermal speed therefore broadens the distribution function of H atoms. In addition, radiation pressure induced by Lyα provides an outward force on H atoms that roughly balances gravity, which prevents significant gravitational focusing of H and causes a longitudinal shift of H with respect to He.

One of the key elements of the observational analysis is the quantitative removal of sputtered He components from the response in ESA 1 and ESA 2. To complete this important step, we analyze the H count rate, R_{oij}, in orbit o, spin-step i, and ESA step j (we focus this analysis only on ESA steps $j = 1$–3). We then take the ratio $\alpha_1 = R_{oi1}/R_{oi3}$, the ratio of the count rates in ESA 1 to ESA 3, and $\alpha_2 = R_{oi2}/R_{oi3}$, the ratio of the count rates in ESA 2 to ESA 3. In orbits such as 64 in 2010, when He strongly dominates the response of *IBEX*-Lo, the ratios α_1 and α_2 indicate the fraction of sputtered H from He in ESA 1 and ESA 2 relative to ESA 3. Since the rate in ESA 3 is dominated by He, the ratios α_1 and α_2 provide a means to estimate the contribution from sputtering to the observed H in ESA 1 and ESA 2. The rate due to ISN H (R_H^p) can then be estimated by

$$R_{oi1}^H = R_{oi1} - R_{oi3}\alpha_1 \quad (1)$$

$$R_{oi2}^H = R_{oi2} - R_{oi3}\alpha_2. \quad (2)$$

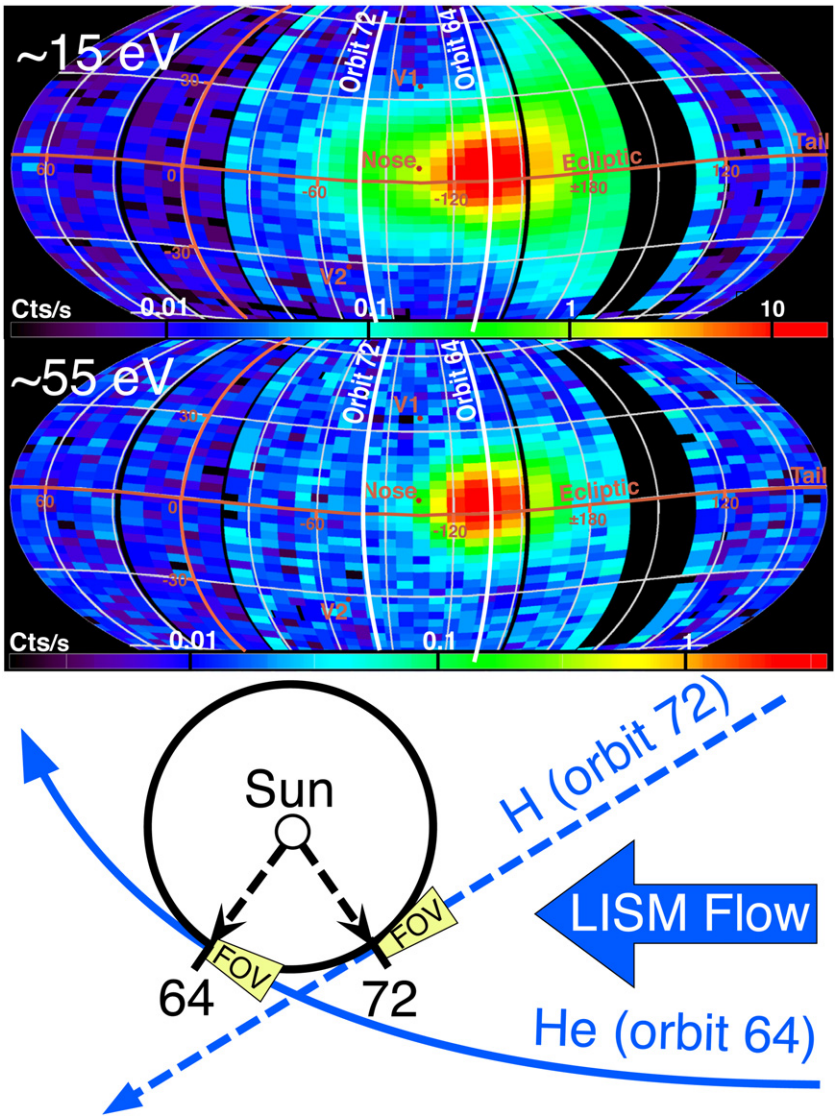

Figure 1. Count rate in ESA 3 (middle panel) on a Mollweide projection (ecliptic coordinates with the nose of the heliosphere as the central longitude) reflects incident LISM He, which peaks in the spring (orbit 64 of 2010, shown by the white curve in the top two panels). The count rate in ESA 1 (top panel) is created by a combination of primary H from the LISM and secondary H sputtered by He. The distribution of H in the top panel at ESA 1 is broader in longitude and in latitude due to the combination of sputtered and primary products as well as the effects of radiation pressure and the larger thermal speed of H atoms. Representative trajectories of He (solid blue curve, bottom panel) and H (dashed blue line, bottom panel) illustrate the importance of radiation pressure, which for H compensates gravity. As a result, only He experiences gravitational focusing, and the *IBEX*-Lo response to H is observed at larger longitudes than the response to He. This result provides the basis for deriving LISM parameters for H by analyzing orbits such as 72 (white curve in the top two panels) where the ISN H atoms dominate the response in ESA 1.

(A color version of this figure is available in the online journal.)

The count-rate ratios of ESA 2/ESA 3 and ESA 1/ESA 3 are shown in Figure 2 as a function of the He incident energy, $E_{\rm He}$, into *IBEX*-Lo. The orbits indicated here are 14 through 19 in 2009 and 59 through 65 in 2010. The ratios appear to bottom out at the highest incident energies. The reason for this behavior is at least in part due to contributions of converted ISN H that become more evident when the He count rate diminishes and the incident He energies fall. There is also, however, likely to be a sputtering efficiency dependence on energy that becomes evident at lower incident He energies. For specificity, we calibrate the efficiency ratios α_1 and α_2 where the He beam is most intense, in orbits 14 through 18 and 61 through 65. We then form an average of the efficiency ratios and derive conservative estimates for the uncertainties based on the minimum and maximum ratios: $\alpha_1 = 0.82 \pm 0.07$ and $\alpha_2 = 0.97 \pm 0.09$. The uncertainties in α_1 and α_2 were estimated in an ad-hoc manner to bound the data points within orbits where the maximum intensity of ISN He was observed. The values of α_1 and α_2 determined in flight tend to be slightly lower than the values inferred from calibration data ($\alpha_1^{\rm cal} = 0.94$ and $\alpha_2^{\rm cal} = 1.16$). We consider the flight data shown in Figure 2 to be the most accurate determination of the sputtering efficiency.

In orbits 23–27 (2009), 70–74 (2010), and 119–123 (2011), we find that converted ISN H dominates sputtered H. We have identified time periods (Table 1) when the backgrounds in these orbits are at low levels. Select time periods that show evidence of background are also removed within these intervals. These backgrounds come from many sources, including solar wind, pickup ions and energetic particles, upwelling ions, and neutrals. The additional backgrounds are suppressed by removing any 64 spin interval with more than 3 counts within 30° of the north ecliptic pole (NEP). Any residual contribution from sputtering is then subtracted from the observed H count rates using Equation (1) for ESA 1 and Equation (2) for ESA 2.

Table 1
IBEX-Lo ISM Observation Periods

Orbit	SunPt Longitude	SW Flux at 1 AU (10^8 cm^{-2} s^{-1})	Good Times for Rates year/m:d:h:m:s–m:d:h:m:s ESA1, ESA 2, ESA3
		2009	
0023	185.95	1.98	2009/03:27:13:51:57–04:02:18:31:42
			2009/03:27:13:36:36–04:02:23:54:07
			2009/03:27:14:22:39–04:02:23:54:07
0024	194.43	1.99	2009/04:07:14:38:46–04:10:15:43:07
			2009/04:04:23:26:55–04:10:15:43:07
			2009/04:04:16:32:44–04:10:15:43:07
0025	201.94	1.95	2009/04:12:02:05:31–04:18:05:45:01
			2009/04:12:03:22:09–04:18:05:45:01
			2009/04:12:02:05:31–04:18:05:45:01
0026	209.35	1.92	2009/04:19:16:13:39–04:25:20:01:15
			2009/04:19:15:58:20–04:25:20:01:15
			2009/04:19:18:46:48–04:25:20:01:15
0027	216.77	1.87	2009/04:27:18:28:42–05:02:23:43:20
			2009/04:27:19:45:13–05:02:23:28:02
			2009/04:27:21:32:21–05:02:23:43:20
		2010	
0070	179.85	1.90	2010/03:21:02:37:28–03:27:07:05:06
			2010/03:20:16:05:37–03:27:07:05:06
			2010/03:20:15:34:48–03:27:07:05:06
0071	187.54	1.91	2010/03:28:22:47:29–04:03:22:30:54
			2010/03:28:15:36:19–04:03:22:30:54
			2010/03:28:20:59:42–04:03:22:30:54
0072	195.08	1.88	2010/04:05:17:16:26–04:11:17:55:22
			2010/04:05:11:07:07–04:11:17:39:59
			2010/04:05:09:34:48–04:11:17:55:22
0073	202.47	1.88	2010/04:13:04:11:19–04:18:16:10:03
			2010/04:13:07:46:35–04:18:20:31:26
			2010/04:13:08:01:57–04:18:18:28:26
0074	209.82	1.89	2010/04:21:03:16:56–04:26:12:05:31
			2010/04:21:02:00:07–04:26:12:05:31
			2010/04:21:01:29:23–04:25:12:05:31
		2011	
0119	187.90	2.06	2011/03:28:16:54:48–04:04:11:38:41
			2011/03:28:16:54:48–04:04:09:20:32
			2011/03:28:16:54:48–04:04:11:38:41
0120	195.26	1.99	2011/04:05:21:36:44–04:12:03:42:33
			2011/04:05:21:21:23–04:12:03:42:33
			2011/04:05:20:35:21–04:12:03:42:33
0121	202.80	2.05	2011/04:13:08:40:39–04:19:21:20:41
			2011/04:13:08:25:19–04:19:21:20:41
			2011/04:13:08:25:19–04:18:21:20:41
0122	210.47	2.09	2011/04:21:03:45:18–04:27:05:04:13
			2011/04:21:03:45:18–04:27:05:04:13
			2011/04:21:03:45:18–04:27:12:43:55
0123	217.73	2.02	2011/04:29:08:47:45–05:04:22:47:01
			2011/04:29:06:29:56–05:05:01:50:46
			2011/04:29:04:42:44–05:04:19:43:15

The resulting H count rates provide the basis for comparison with the modeled count rates (Lee et al. 2012). The uncertainties in H count rates are determined from Poisson statistics of the observed rates and the propagation of uncertainties in α_1 and α_2.

3. COMPARISONS BETWEEN THE OBSERVATIONS AND THE MODEL

The simulated count rates shown here are based on the Lee et al. (2012) model generalized for $\mu > 1$, as detailed in Appendix A. The model provides the distribution function of neutral atoms at *IBEX* and accounts for propagation and ionization effects in the supersonic solar wind. This distribution function of neutrals is then integrated over the *IBEX*-Lo response function to simulate the sensor count rates as a function of ESA step and spin-phase angle (i.e., the spin angle of the sensor with respect to the NEP). This methodology allows us to make direct comparisons between results of the model and the observed count rates.

The Lee et al. (2012) model utilizes a reference Maxwellian distribution at the termination shock with a given ISN H flow

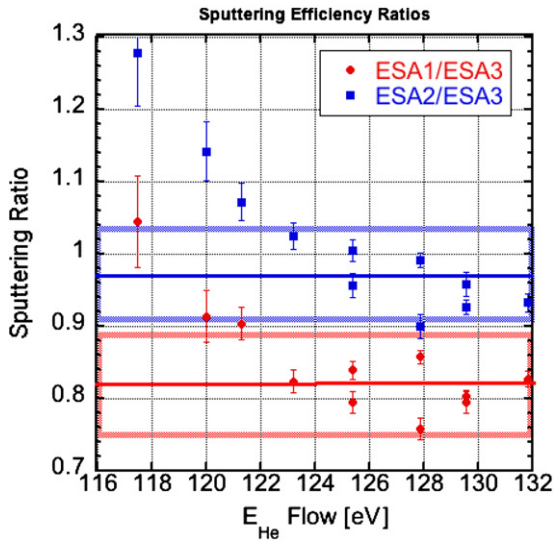

Figure 2. Count-rate ratios of ESA 1/ESA 3 (red) and ESA 2/ESA 3 (blue) during periods when the *IBEX*-Lo response to He is the most intense. These count-rate ratios are used to determine the sputtered H count rate in ESA steps 1 and 2 based on the count rate in ESA 3 (see Equations (1) and (2)). Shown here are these count-rate ratios for orbits 14 through 19 in 2009 and orbits 59 through 65 in 2010 as a function of the incident He energies into *IBEX*-Lo. The means of the efficiency ratios from orbit 14 through 18 and 61 through 65 are shown by solid lines and uncertainties are indicated with the upper and lower light bounding lines.

(A color version of this figure is available in the online journal.)

velocity, density, and temperature. As illustrated in Figure 1, we analyze orbits where ISN H dominates over ISN He. This specific data selection includes observations of ISN H atoms that originate from longitudes greater than that of the nose of the heliosphere. Therefore, the parameters for ISN H that we derive from comparisons between the model and the *IBEX* observations represent the ISN H properties in specific regions (longitudes greater than that of the nose) at the termination shock.

The integrated rate in a given orbit o, at a given ESA step i (i ranges from 1 to 8) and spin-sector j for *IBEX*-Lo, is

$$\tilde{R}_{oij} = \frac{1}{t_1 - t_0}\int_{t_0}^{t_1} dt \frac{1}{\Delta\xi}\int_{\xi_j-\Delta\xi/2}^{\xi_j+\Delta\xi/2} d\xi \times \int dE \int d\alpha' \int d\beta' J(E,\alpha',\beta') \times G_i E P(\alpha',\beta') T(E - E_i), \quad (3)$$

where time t ranges from t_0 and t_1, and the spin phase ξ spans the range from $\xi_j - \Delta\xi/2$ to $\xi_j + \Delta\xi/2$ and is centered on the spin-phase center (ξ_j). The spin-phase bin width is $\Delta\xi = 6°$. The differential flux is in the *IBEX* reference frame is $J(E,\alpha',\beta')$, which depends on the energy E in the *IBEX* frame and the acceptance angles (α',β'). The energy integral extends over the transmission function $T(E - E_i)$, which is approximately a Gaussian with FWHM that is ~70% of the central energy E_i. The geometric factor G_i has units of cm^2 sr eV/eV. The point spread function $P(\alpha',\beta')$ for *IBEX*-Lo represents the angular acceptance function as a function of ENA incidence angles (α',β') and is detailed by Schwadron et al. (2009). The transmission function has been determined using a functional

Table 2
Hydrogen Energies in the Transmission Function of *IBEX*-Lo in ESA Steps 1 and 2

ESA Step	E_c (eV)	E_- (eV)	E_+ (eV)
1	15	11	21
2	29	20	41

fit to the calibration data and is given by

$$T(E) = \exp\left(-4\ln 2\frac{(E/E_c - 1)^2}{\Delta_1^2}\right) \quad \text{for } E \leqslant E_c$$
$$= \exp\left(-4\ln 2\frac{(E_c/E - 1)^2}{\Delta_2^2}\right) \quad \text{for } E > E_c, \quad (4)$$

where E_c is the central energy of a given ESA step. The width $\Delta_1 = 2(1 - E_-/E_c)$ is the half-max for energies less than the central energy. Similarly, $\Delta_2 = 2(1 - E_c/E_+)$ is the half-max for energies greater than the central energy. The central energies, E_- and E_+, are listed in Table 2.

The force associated with the radiation pressure divided by the gravitational force, μ, depends on the Lyα line profile. Atoms with different radial velocities are Doppler shifted and therefore experience different amounts of radiation pressure, which depends on the precise form of the Lyα profile.

Measurements of the solar Lyman-line profile have been made for many decades (Vidal-Madjar 1975; Artzner et al. 1978; Bonnet et al. 1978; Lemaire et al. 1978; Woods et al. 1995). These Lyα measurements were performed from within Earth's exosphere and were therefore affected by absorption from geocoronal hydrogen. The *Solar and Heliospheric Observatory* (*SOHO*) orbits the L first Lagrange point, providing the first unobstructed view of the disk-integrated solar line (Warren et al. 1998; Lemaire et al. 1998, 2002, 2005). These measurements make it possible to observe the Lyα profile during all solar activity phases from solar minimum to solar maximum.

The solar Lyα line features a self-reversed shape that has been approximated by two Gaussian functions (Fahr 1979; Chabrillat & Kockarts 1997; Scherer et al. 2000). Tarnopolski & Bzowski (2009) fit measurements by Lemaire et al. (2002) with a three-Gaussian model parameterized by the disk-integrated flux. We utilize here a similar parameterization (see Bzowski et al. 2013):

$$\mu(v_r) = \mu_0 \exp\left(-Cv_r^2\right)\left[1 + (1+\gamma)\left\{D\exp\left(Fv_r - Gv_r^2\right) + H\exp\left(-Pv_r - Qv_r^2\right)\right\}\right][1 + (D+H)(1+\gamma)]^{-1}, \quad (5)$$

where $C = 3.831 \times 10^{-5}$, $D = 0.73879$, $F = 4.0396 \times 10^2$, $G = 3.5135 \times 10^4$, $H = 0.47817$, $P = 4.6841 \times 10^2$, and $Q = 3.3373 \times 10^4$. Note that v_r is expressed in km s^{-1}. The only departures from the three-Gaussian model are that (1) we normalize the radiation pressure by μ_0, defined here as the radiation pressure divided by gravity for a particle with $v_r = 0$; and (2) the parameter γ raises the wings of Lyα, as shown in Figure 3. The variation with γ leads to changes in μ for particles with speeds of ~50–120 km s^{-1}. The variation in γ therefore significantly affects the modeled count rates from ESA 2.

The parameter μ_0 can be related in the three-Gaussian model to the integrated Lyα flux ($I_{\rm tot}$) by

$$\mu_0 = A(1 + BI_{\rm tot})(1 + D + H), \quad (6)$$

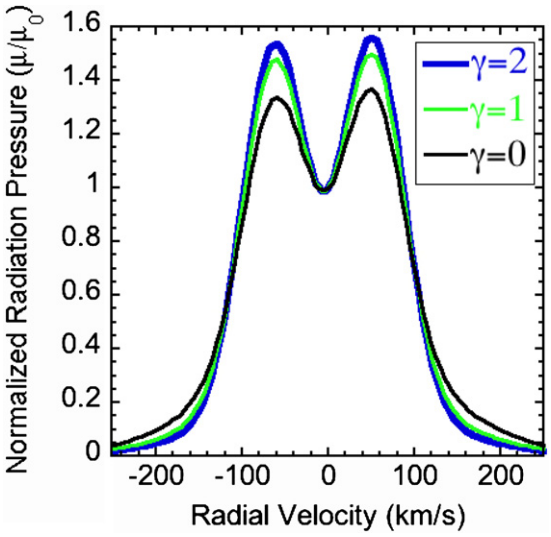

Figure 3. Basic radiation pressure model used here, based on Bzowski et al. (2011). These authors use a fitting function (5) for the solar Lyα profile. The shape of the μ profile shown here directly reflects the shape of the Lyα line. The height of the wings of the distribution vary slightly based on the parameter γ. The variation with γ leads to changes in μ for particles with speeds of ~50–120 km s^{-1}. The variation in γ therefore significantly affects the modeled count rates from ESA 2. A number of different parameter choices for γ are shown here for the radiation pressure divided by a reference value (μ_0) as a function of the radial velocity of H atoms. Note, in particular, that the atoms with radial velocities ~60 km s^{-1} experience the largest effects of radiation pressure.

(A color version of this figure is available in the online journal.)

where $A = 2.4543 \times 10^{-9}$, $B = 4.5694 \times 10^{-4}$, and $I_{\rm tot}$ is expressed in cm^{-2} s^{-1}. The exact shape of the Lyα profile and the Lyα flux with time are both subject to uncertainty. As such, the parameters μ_0 and γ allow for varying effects of radiation to provide best fits between the results of the model and the *IBEX* observations.

An important component of the Lee et al. (2012) model is ionization that results in the loss of some atoms as they move through the inner heliosphere. The survival probability for an H atom, S_p, represents the probability that the atom survives as a neutral atom along its trajectory to the *IBEX* satellite:

$$S_p = \exp\left(-\int_{-\infty}^{t} dt' \nu(t')\right), \tag{7}$$

where the ionization rate is

$$\nu = F_{\rm sw}\sigma + \nu_{\rm photo}, \tag{8}$$

$F_{\rm sw}$ is the flux of the solar wind, σ is the charge exchange cross section, and $\nu_{\rm photo}$ is the photoionization rate. Note that the cross section σ depends on the energy of the incident neutral atoms. In the modeling here, we solved for the survival probability by integrating backward in time over atom trajectories and taking into account the changing flux in the solar wind based on our 1 AU observations.

At a given point along an atom's trajectory, we specify the solar wind flux assuming a uniform latitudinal and longitudinal distribution of solar wind and a solar wind flux that falls off as r^{-2}, where r is radial distance. While the model is crude, it is an appropriate approximation along an atom's time history that takes years to propagate through the inner heliosphere. To quantify the results of the backward integration, we form a reference 1 AU flux, $\tilde{F}_{\rm sw}$, which is defined as

$$\tilde{F}_{\rm sw} = \left[\int_{-\infty}^{t} dt' F'_{\rm sw}\right]\left[\int_{-\infty}^{t} dt'(R_1/r')^2\right]^{-1}, \tag{9}$$

where $F'_{\rm sw}$ is the flux of the solar wind at time t' and radial position r' along the neutral atom's backward-integrated trajectory. We project out the solar wind flux observed at 1 AU at time t, $F_{\rm sw-1}(t)$, at an average radial speed of $V_{\rm sw} = 450$ km s^{-1} to solve for the solar wind flux along the neutral atom's trajectory:

$$F_{\rm sw}(t', r') = F_{\rm sw-1}[t = t' - (r' - R_1)/V_{\rm sw}] \times \left[\frac{R_1}{r'}\right]^2. \tag{10}$$

Here, R_1 is 1 AU. The reference 1 AU solar wind flux $\tilde{F}_{sw}$ depends on the time of observations and therefore varies throughout the orbits studied here. We find that the 1 AU reference flux is $\tilde{F}_{sw} \approx 2 \times 10^8$ cm^{-2} s^{-1}. Column 3 of Table 1 lists the reference 1 AU solar wind flux for each of the orbits studied here.

The charge-exchange rate, which is controlled largely by the flux of the solar wind, is almost a decade larger than the photoionization rate. Nonetheless, the photoionization rate is an important factor. Following the Lee et al. (2012) model, the photoionization rate is taken as

$$\nu_{\rm photo} = \nu^0_{\rm photo}\left(\frac{R_1}{r}\right)^2, \tag{11}$$

where R_1 is again 1 AU and $\nu^0_{\rm photo}$ is the photoionization rate at 1 AU. Based on the results of Bzowski et al. (2011), we take a photoionization of $\nu^0_{\rm photo} = 8 \times 10^{-8}$ s^{-1} in 2009 (orbits 23–27), $\nu^0_{\rm photo} = 8.5 \times 10^{-8}$ s^{-1} in 2010 (orbits 70–74), and $\nu^0_{\rm photo} = 9.4 \times 10^{-8}$ s^{-1} in 2011 (orbits 119–123).

Combining the photoionization rate with the backward integrated charge-exchange rate, we express the ionization rate as

$$\nu = \tilde{\nu}^0\left(\frac{R_1}{r}\right)^2, \tag{12}$$

where $\nu^0 = \tilde{F}_{\rm sw}\sigma + \nu^0_{\rm photo}$. Following the formalism from Lee et al. (2012), the angular rate of change along an atom's trajectory is $\dot{\theta} = -l/(mr^2)$, where l is the angular momentum and m is the neutral atom's mass. Therefore, substituting the angular rate of change into the formula for the survival probability (7), we can evaluate the integral for the survival probability explicitly,

$$S_p = \exp\left(mR_1^2\tilde{\nu}^0 l^{-1}[\theta - \theta_\infty]\right), \tag{13}$$

where θ is the position angle at the time of observation (see Appendix A) and θ_∞ is the position angle when the neutral was far from the Sun (at $t = -\infty$), as defined by Lee et al. (2012). At the point of observation, the neutral atom has a position **R** with respect to the Sun and a velocity **V**. The cosine of the atom's azimuthal angle is $\cos\phi = -\mathbf{R}\cdot\mathbf{V}/(RV)$. For $\phi < \pi/2$, the position angle is $\theta = 0$; for $\phi \geqslant \pi/2$, $\theta = -2|\theta_0|$, where $-\theta_0$ is the position angle at perihelion (Appendix A).

ISN H densities at the termination shock have been studied extensively using wide-ranging techniques, which were discussed

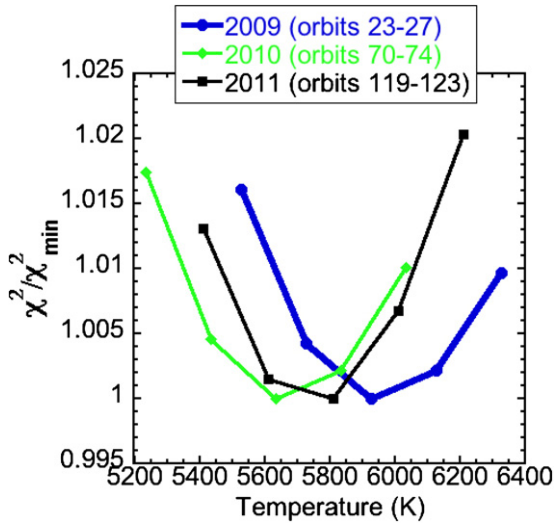

Figure 4. χ^2 normalized by its minimum as a function of inner heliosheath temperature with all other parameters at the χ^2 minimum values listed in Table 3. The three curves show the variation of χ^2 in the 2009 (blue), 2010 (green), and 2011 (black) data. We see here and with four other parameters (excepting γ) that χ^2 is indeed minimized.

(A color version of this figure is available in the online journal.)

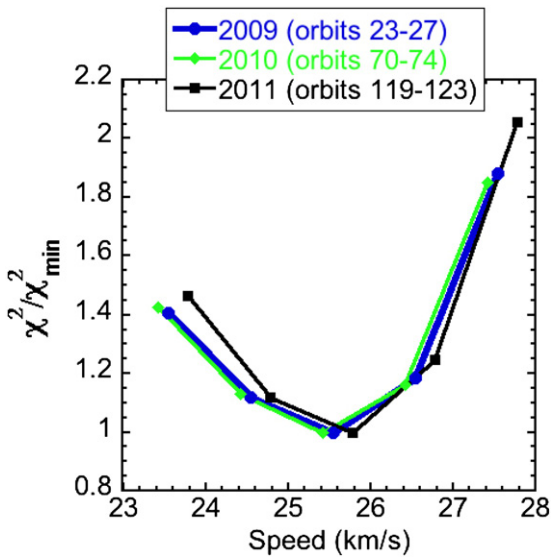

Figure 5. Normalized χ^2 as a function of the speed of ISN H in the inner heliosheath. All parameters other than speed are held at the χ^2 minimum values listed in Table 3.

(A color version of this figure is available in the online journal.)

extensively at an International Space Science Institute workshop in 2008 (Bzowski et al. 2008; Möbius 2009). Values for the neutral H density between 0.08 cm^{-3} and 0.085 cm^{-3} were found, with a ~25% uncertainty. Möbius (2009) concluded a density of 0.083 ± 0.023 cm^{-3} based on a weighted mean of disparate results and a conservative uncertainty range. Bzowski et al. (2008) found a density of 0.087 ± 0.022 cm^{-3} based on *Ulysses* pickup ion observations. Bzowski et al. (2009) took into account a wide array of relevant determinations and consolidated results for a density of 0.09 ± 0.022 cm^{-3}. In the ISN H modeling performed here, a density of 0.08 cm^{-3} provides the best overall fit to the observations and is clearly within the wide uncertainty range of the results (Bzowski et al. 2008; Möbius 2009; Bzowski et al. 2009).

In addition to the parameters already listed that have been determined based on results of previous studies (e.g., ionization rates and the density of ISN H), there are six additional parameters that must be specified in the model: μ and γ, which characterize the effects of radiation pressure, the speed and temperature of inflowing H atoms from the inner heliosheath, and the longitudinal and latitudinal directions of the flow of H atoms in the inner heliosheath. These six parameters are determined based on a non-linear least squares fitting method (chapter 15 of Press et al. 1992). Specifically, we utilize the Levenberg–Marquardt method (Marquardt 1963) to minimize χ^2, defined as

$$\chi^2(\mathbf{a}) = \sum_{o=\text{orbits}} \sum_{j=1}^{2} \sum_{i=8}^{23} \left[\frac{R^H_{oij} - \tilde{R}_{oij}}{\sigma^H_{oij}} \right]^2, \qquad (14)$$

where $(\sigma^H_{oij})^2$ is the variance associated with the ISN H count rate, R^H_{oij}, and $\mathbf{a}$ is the vector of six free parameters.

It is important to recognize one of the limitations of the Lee et al. (2012) model: it does not take into account time variations. Both the ionization rates and radiation pressure fall off as $1/R^2$. A particle moving at ~25 km s^{-1} requires about four months to move out to a radial distance of 2 AU (taking into account that *IBEX* views atoms roughly perpendicular to the almost Sun-pointed spin-axis). Therefore, the radiation pressure and ionization rates in the model can be approximated by four month averages of these quantities. In addition, the radiation pressure is a function only of a particle's radial speed. Due to the *IBEX* viewing geometry with the *IBEX*-Lo boresight almost perpendicular to the roughly Sun-pointing spin vector, the radial velocity of accepted neutrals is almost zero near the spacecraft. When a particle was at ~2 AU, the radial speed was ~87% of the total speed. Beyond 2 AU, the radial component of the particle velocity converges to the total speed. Therefore, the radial component of the particle speed falls rapidly inside 2 AU, which biases μ to μ_0. These considerations complicate interpretations from the analytic model and highlight the need for further numerical modeling that takes into account detailed time dependence and the radiation pressure's dependence on the changing radial velocity component as the neutrals approach the spacecraft.

Table 3 shows the parameters derived from the χ^2 minimization. Except for γ, all the parameters are associated with local minima. For γ, however, the minimum appears near $\gamma = 2$, which is the upper end of the range over which the parameter can be varied. The reduced χ^2 (χ^2 divided by the number of free parameters) is shown as a function of the temperature (Figure 4), speed (Figure 5), μ (Figure 6), the longitudinal direction of the ISN H inflow in the heliosheath (Figure 7), and the latitudinal direction of the ISN H inflow in the heliosheath (Figure 8).

Figures 9–11 directly compare the results of the model with the observations in the orbits during 2009 (Figure 9), 2010 (Figure 10), and 2011 (Figure 11). Generally, the agreement appears reasonable. However, there are significant differences between the model and the observations that will need to be reconciled in future studies. The comparison shown here is a first step, but by no means the final result of the analysis of these data from *IBEX*-Lo.

The results of the modeled count-rate distributions show a pronounced dependence on the inflow latitude, which causes

Table 3
Derived Parameters Associated with ISN H from Reduced χ^2 Minimization

Year	Orbits	μ	Speed V (km s^{-1})	Temp. T (K)	Ec. Long. λ (°)	Ec. Lat. Ψ (°)	γ	Min.[a] $(\chi')^2$
2009	23–27	0.94 ± 0.04[b]	25.5 ± 0.9[b]	5900 ± 400[b]	79.5 ± 1.2[b]	-3.0 ± 0.5[b]	2.0 ± 1.0[b]	5.6
		± 0.03[c]	± 0.9[c]	± 300[c]	± 1.1[c]	± 0.2[c]	± 0.3[c]	
		± 0.007[d]	± 0.2[d]	± 200[d]	± 0.5[d]	± 0.4[d]	± 0.9[d]	
2010	70–74	0.93 ± 0.03[b]	25.4 ± 0.7[b]	5600 ± 500[b]	74.7 ± 1.0[b]	-4.3 ± 0.5[b]	1.9 ± 0.5[b]	8.2
		± 0.03[c]	± 0.7[c]	± 400[c]	± 0.8[c]	± 0.2[c]	± 0.2[c]	
		± 0.007[d]	± 0.2[d]	± 200[d]	± 0.5[d]	± 0.5[d]	± 0.4[d]	
2011	119–123	1.01 ± 0.05[b]	25.8 ± 0.8[b]	5800 ± 500[b]	76.5 ± 1.3[b]	-2.5 ± 0.4[b]	2.0 ± 0.6[b]	2.5
		± 0.05[c]	± 0.8[c]	± 400[c]	± 1.2[c]	± 0.3[c]	± 0.6[c]	
		± 0.01[d]	± 0.2[d]	± 200[d]	± 0.5[d]	± 0.3[d]	± 0.1[d]	
Average[e]		0.95 ± 0.03	25.6 ± 0.5	5800 ± 260	76.5 ± 1.6	-3.2 ± 0.6	1.9 ± 0.3	

Notes.
[a] $(\chi')^2 = \chi^2/M$ with $M = 154$ degrees of freedom.
[b] Uncertainty of mean = root square sum of the fit uncertainty and the propagation uncertainty.
[c] Fit uncertainty (Appendix B).
[d] Propagation uncertainty.
[e] Averages and uncertainties based on statistics of the mean (Appendix C).

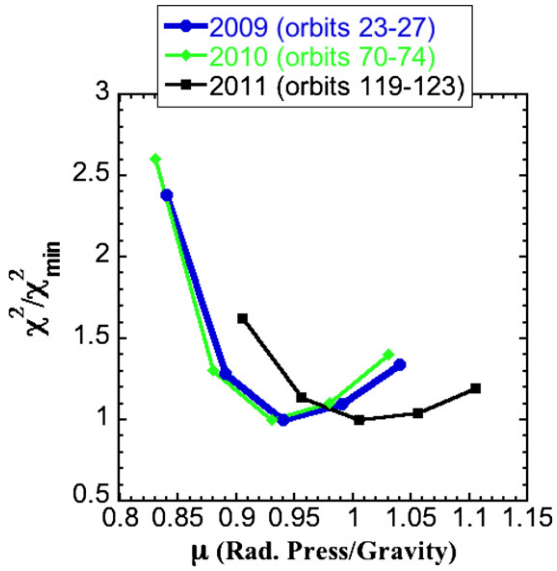

Figure 6. Normalized χ^2 as a function of μ, the radiation pressure divided by gravity. All parameters other than μ are held at the χ^2 minimum values listed in Table 3.
(A color version of this figure is available in the online journal.)

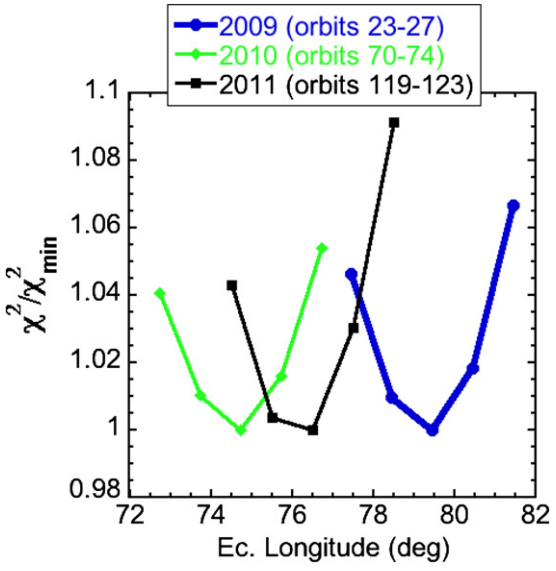

Figure 7. Normalized χ^2 as a function of the inflow longitude direction of the ISN H in the inner heliosheath. All parameters other than the inflow longitude are held at the χ^2 minimum values listed in Table 3.
(A color version of this figure is available in the online journal.)

the count rate to be asymmetric with respect to the NEP. This asymmetry is clear in Figures 9–11, where the peaks in the count-rate distributions are at spin angles less than 90°. This same asymmetry is manifested in the observed count-rate distributions, which results in negative inflow latitudes (directed below the ecliptic) from the χ^2 fits in each of the three years from 2009–2011.

Möbius et al. (2012) and Bzowski et al. (2012) showed, from the determination of ISN He parameters from *IBEX*-Lo observations, that there are well-defined relationships between velocity, temperature, latitude, and ecliptic longitude that are evident in the χ^2 dependence of these parameters. In particular, the speed and temperature as a function of ecliptic longitude introduce significant degeneracy in the χ^2 minimization. However, in the search for the ISN H parameters, an equivalent degeneracy appears to be largely absent. Figure 12 shows normalized χ^2 as a function of speed, temperature, and ecliptic longitude. The local minima in χ^2 are isolated and do not conform to the degenerate functions found in the study of ISN He parameters.

There are two types of uncertainties listed in Table 3. Statistical uncertainties are the result of propagation of error, as indicated in Press et al. (1992). Fitting uncertainties are derived from the results of χ^2, as detailed in Appendix B. The root square sum of these uncertainties yields the total uncertainty for the fit parameters in each year. The final averages and *total* uncertainties are listed on the bottom row of Table 3 using the statistics of the mean summarized in Appendix C.

4. DISCUSSION

We have compared the *IBEX*-Lo H observations from 2009–2011 with the simulated results from the model of Lee

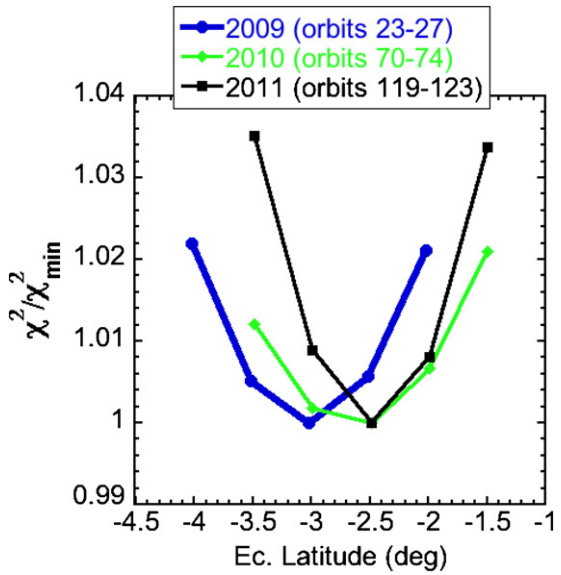

Figure 8. Normalized χ^2 as a function of the inflow latitude direction of the ISN H in the inner heliosheath. All parameters other than inflow latitude are held at the χ^2 minimum values listed in Table 3.

(A color version of this figure is available in the online journal.)

et al. (2012), which treats the propagation and loss of neutral atoms within the termination shock. We have derived flow parameters for the incoming distribution of H atoms near the termination shock.

The parameters derived from the non-linear least squares fitting are compared with the ISN He parameters listed in Table 4. Generally, the comparison reveals that the ISN H temperature is similar to the ISN He temperature, but smaller by ∼500 K. The speed of ISN H is similar to the ISN He speed, but ∼2.4 km s^{-1} larger. These signatures suggest that our observations reflect the properties of the primary component of

Table 4
Comparison of ISN H Parameters with ISN He Parameters from IBEX

Parameter	ISN He[a]	ISN H
Speed V (km s^{-1})	23.2 ± 0.3	25.6 ± 0.5
Temp. T (K)	6300 ± 390	5800 ± 260
Ec. Long. λ (°)	79.00 ± 0.47	76.5 ± 1.6
Ec. Lat. Ψ (°)	−4.98 ± 0.21	−3.2 ± 0.3

Note. [a] He parameters from McComas et al. (2012).

ISN H coming directly from the LISM and flowing through the heliosphere.

Bzowski et al. (2008) showed that an important by-product of the filtration process in the outer heliosheath is the preferential loss of slower atoms in the distribution of ISN H. This process leads to a ∼2–3 km s^{-1} increase in the average speed of the ISN H and a ∼300–400 K decrease in the temperature of ISN H at the termination shock compared with the parameters of neutral H in the LISM. These signatures of filtration are consistent both with the fact that the ISN H atoms have a bulk speed ∼2.4 km s^{-1} faster and a ∼500 K lower temperature than ISN He.

In addition to the primary component of ISN H, there should also be a slower and more heated secondary component of ISN H revealed by *SOHO*/SWAN observations (Quémerais et al. 1999; Lallement et al. 2005; Costa et al. 1999) and simulations (Izmodenov et al. 2003). However, the ISN H speed is too fast and the temperature is far too low to be consistent with the secondary component.

The missing secondary component presents an important challenge to our understanding of the interactions in the outer heliosheath. However, the *IBEX*-Lo observations analyzed here cover a limited longitude range on the termination shock. We quantify the characteristic longitudinal source region on the termination shock using the Lee et al. (2012) ISN model.

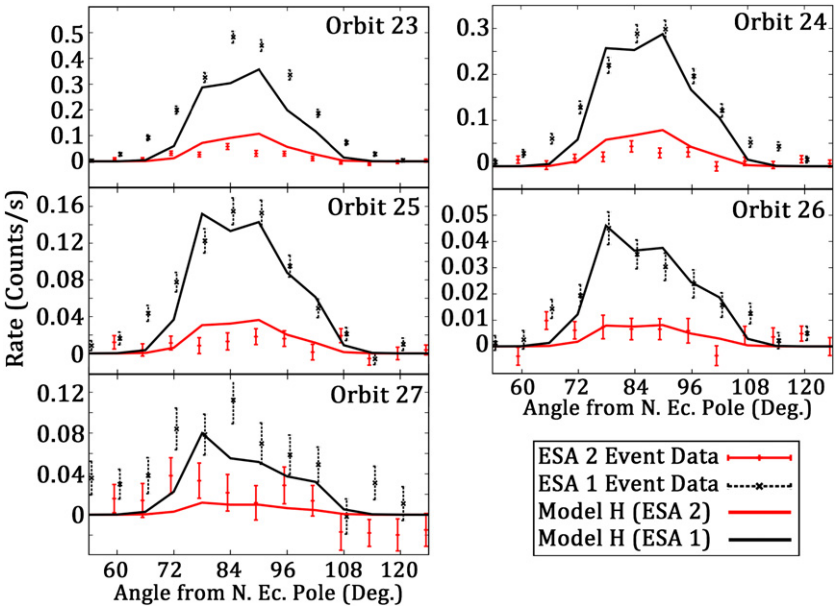

Figure 9. Comparison between the observations and the model for ISN H in 2009 during orbits 23 through 27. The rates shown here are corrected for contributions from sputtering by He based on Equation (1). The data points (black for ESA step 1 and red for ESA step 2) show observed the rates, while the curves show the results of the model.

(A color version of this figure is available in the online journal.)

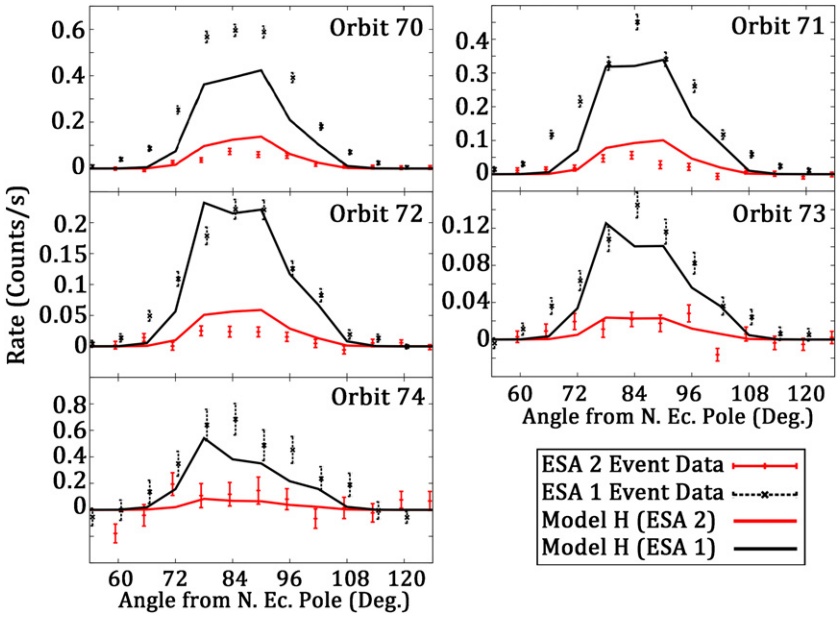

Figure 10. Comparison between the observations and the model for ISN H in 2010 during orbits 70 through 74.
(A color version of this figure is available in the online journal.)

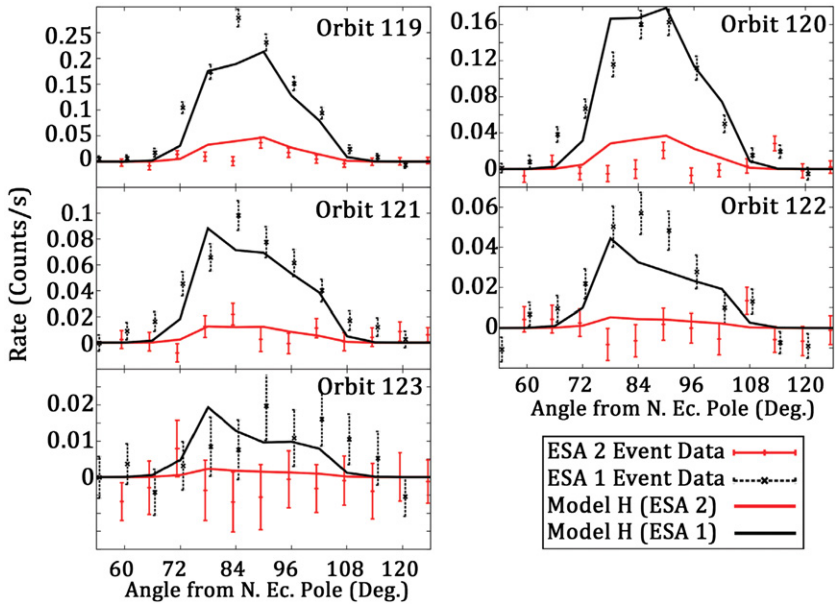

Figure 11. Comparison between the observations and the model for ISN H in 2011 during orbits 119 through 123.
(A color version of this figure is available in the online journal.)

The deviation angle (θ_∞) of inflowing H atoms is

$$\cos(\theta_\infty) \approx -\left(\frac{V^2 R_0}{G M_s(1-\mu)} + 1\right)^{-1}, \qquad (15)$$

where V is the average speed of inflowing ISN H atoms at the termination shock, R_0 is 1 AU, G is the gravitational constant, and M_s is the solar mass. For a typical speed $V = 25.6$ km s^{-1} and $\mu = 1.1$, we find that $\theta_\infty \approx 80°$. The longitude of the origin (λ_∞) on the termination shock is $\lambda_\infty = \lambda_{\rm sunPt} + \theta_\infty$, where $\lambda_{\rm sunPt}$ is the Sun-pointing longitude of the spacecraft where the spacecraft's spin-axis points toward the Sun (second column of Table 1). Based on the Sun-pointing longitudes in Table 1, we find the longitudes of the origin on the termination shock. We therefore show the contributions to $(\chi')^2$ from each of the orbits as a function of the longitude of the origin (Figure 13). The heliospheric nose for ISN H is $\lambda_{\rm nose} \sim 256.^\circ5$, based on the observations reported here.

We observe in Figure 13 that there are increasing departures from the model as the longitudes of the origin approach the nose. This trend is consistent with the existence of a secondary component absent from our model that contributes additional neutrals from near the nose of the heliosphere. Therefore, longitudinal variation of ISN H parameters may be evident in the observations shown here.

A recent study by Zieger et al. (2013) may shed some light on the origin of the secondary component of ISN H. Zieger et al. (2013) modeled the outer heliosheath in the presence of a strong

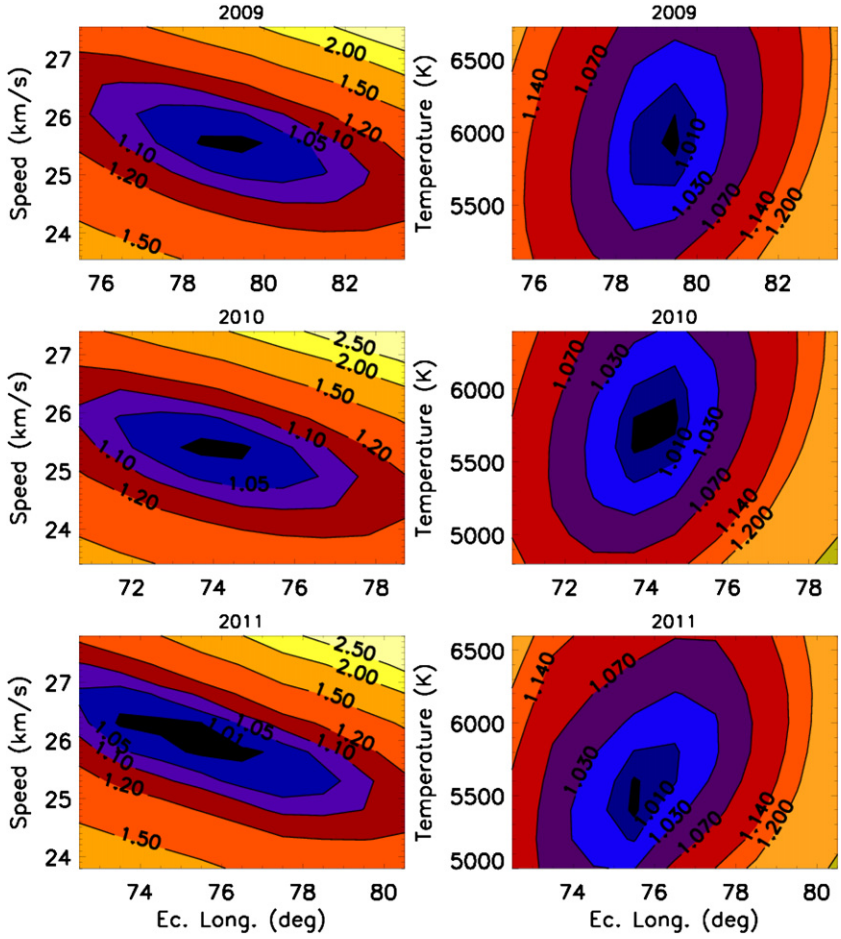

Figure 12. Two-dimensional χ^2 distributions in speed (left panels) and temperature (right panels) vs. ecliptic longitude show well-defined minima. The bulk speed (left panels), temperature (right panels), and ecliptic longitude are varied with the remaining parameters μ, γ, and ecliptic latitude held at their respective χ^2 minimum values. The χ^2 values are normalized by the respective minima defined in Table 3. The contours are labeled with their respective values of $\chi^2/\chi^2_{\rm min}$. The results from 2009, 2010, and 2011 are shown in the first, second, and third rows, respectively.

(A color version of this figure is available in the online journal.)

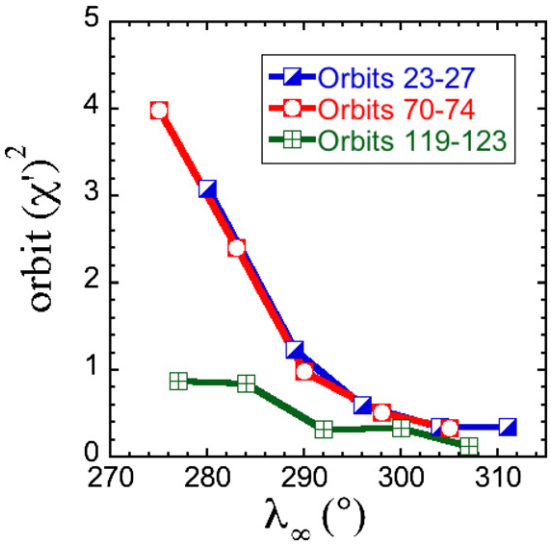

Figure 13. Contributions to $(\chi')^2$ from each of the orbits in successive years as a function of longitude of the origin (λ_∞) reveal that the most significant departures from the model are at the lowest values of λ_∞. The heliospheric nose is at 256.°5. Therefore, we observe increasing departures from the model as the longitude of the origin approaches the heliospheric nose. This behavior is likely explained by the secondary component of H from the heliosheath.

(A color version of this figure is available in the online journal.)

4.37 μG local interstellar magnetic field, which induces a slow bow shock over a limited region of the outer heliosheath. Of particular significance is that the slow bow shock forms over a range of longitudes *smaller* than the nose longitude. In the range of longitudes larger than that of the nose, where we infer ISN H parameters, the compression in the outer heliosheath exists over a more limited radial range and should result in a smaller flux from the secondary component. The implication is that the interaction of LISM H likely varies depending on where H atoms propagate through the outer heliosheath. As a result, the distribution of secondary atoms and the nature of filtration may have significant directional (longitudinal and latitudinal) variations. More specifically, we expect to see a larger secondary component for longitudes of the origin that are similar to and smaller than the nose longitude. This trend appears to be present in Figure 13: departures from the modeled primary component increase as the observations scan smaller longitudes of the origin that approach the nose longitude.

Figure 14 compares the evolution of the derived μ parameter (radiation pressure over gravity) in 2009, 2010, and 2011 with the results of Bzowski et al. (2011) for radiation pressure derived from Lyα observations. The agreement is apparent. In particular, *IBEX*-Lo appears to observe the increase in μ as the solar activity increases.

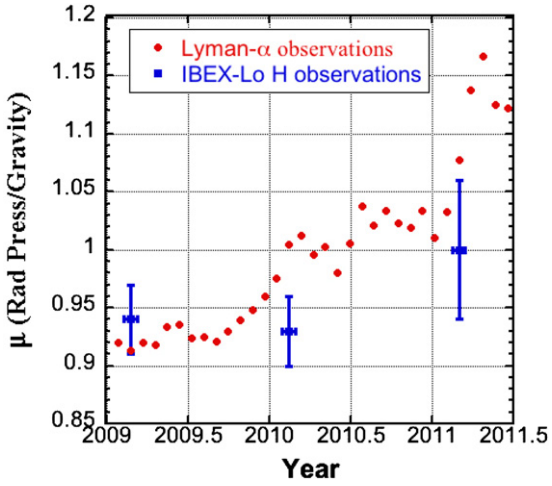

Figure 14. Comparison of the μ parameter (radiation pressure over gravity) derived here (blue points) with the results of Bzowski et al. (2011) based on Lyα observations (red points).

(A color version of this figure is available in the online journal.)

Thus, we show the first quantitative comparison between *IBEX*-Lo observations of interstellar neutral H and an analytic model. The results of the model show that the ISN H observations are consistent with primary incoming LISM H atoms that are filtered in the outer heliosheath. In addition, we derive estimates of the radiation pressure that are consistent with inferences based on Lyα observations. The observational periods that were studied are consistent primarily with incoming atoms that arrive from regions adjacent to and at larger longitudes than the nose of the heliosphere.

We are deeply indebted to all of the outstanding people who made the *IBEX* mission possible. This work was carried out as a part of the *IBEX* project, with support from NASA's Explorer Program and the Polish Ministry for Science and Higher Education (grant NS-1260-11-09). Support for M.B. was also provided by the Polish Ministry for Science and Higher Education grant N-N203-513-0938, managed by the Polish National Science Centre.

APPENDIX A

MOTION OF NEUTRAL ATOMS INFLUENCED BY SOLAR GRAVITY AND RADIATION PRESSURE FOR $\mu > 1$

The treatment of neutral H in this paper requires that we take into account the effects of radiation pressure on neutral atoms. Lee et al. (2012) developed an analytical method for solving for the distribution function of neutral atoms that we utilize here (Equations (1)–(8) from Lee et al. 2012). However, the treatment applies for $\mu < 1$ (where μ is the radiation pressure divided by the gravitational force). Here, we develop the specific revisions to the Lee et al. (2012) formulae needed for the solution in the limit $\mu > 1$.

We start by reviewing the formula for an atom's kinetic energy,

$$E = mV^2/2 - k/R, \tag{A1}$$

where $k = GmM_s(1-\mu)$, G is the gravitational constant, m is the atom mass, M_s is the solar mass, and μ describes the ratio of radiation pressure to gravity. The speed of the atom far from the Sun is $V_\infty = \sqrt{2E/m}$. The angle between $\mathbf{R}$ and a position vector along the trajectory $\mathbf{R}(t)$ is θ. The angle θ_∞ corresponds to the position of the particle as it approaches the heliosphere far from the Sun ($\mathbf{R}(t \rightarrow -\infty)$) and the angle $\theta = -\theta_0$ is at perihelion, the position closest to the Sun. The angle ϕ is defined by $\cos\phi = -\mathbf{R}\cdot\mathbf{V}/(RV)$.

There is one essential revision to the Lee et al. (2012) formulae to account for $\mu > 1$:

$$\frac{1}{R} = \frac{m|k|}{l^2}[\epsilon\cos(\theta+\theta_0) + \mathrm{sgn}(k)], \tag{A2}$$

where the sign operator is $\mathrm{sgn}(k) = 1$ for $k > 0$ and $\mathrm{sgn}(k) = -1$ for $k < 0$, and is introduced to account for the situation where $\mu > 1$. The angular momentum l is $l = mRV\sin\phi$ and the eccentricity ϵ is given by

$$\epsilon^2 = 1 + \frac{2l^2E}{mk^2}. \tag{A3}$$

Note that $\epsilon > 1$ in all cases since the energy must be a positive value.

The case of $\mu = 1$ leads to $k = 0$ in which the trajectories of atoms become perfectly straight and their kinetic energies do not change along the trajectory. The formalism given here and in Lee et al. (2012) does not treat this case explicitly. However, the formulae in Lee et al. (2012) in the limit that $\mu \rightarrow 1$ converge to the appropriate limiting solution.

The perihelion angle is found from Equation (A2) by setting $\theta = 0$ and may be expressed in a form identical to that in Lee et al. (2012),

$$\theta_0 = \mathrm{acos}\left(\left[\frac{l^2}{m|k|R_0} - 1\right]\Big/\epsilon\right), \tag{A4}$$

where R_0 is the perihelion radial distance from the Sun and $\mathrm{sgn}(\theta_0) = \mathrm{sgn}(\pi/2 - \phi)$. Furthermore, the expression for θ_∞ may also be expressed in a form identical to Lee et al. (2012).

APPENDIX B

ESTIMATION OF PARAMETER FITTING UNCERTAINTIES

In this appendix, we provide the formulae that give the fitting uncertainties in the optimal parameters derived from χ^2 minimization. The fitting of a model to data is achieved through a non-linear least-squares method. This method is applied to a given curve $f(x)$ or data set $\{f_i = f(x_i)\}$ for $i = 1\ldots N$ and a statistical model, $V(x;\, p)$ or $\{V_i(p) = V(x_i;\, p)\}$ for $i = 1\ldots N$. The fitting involves finding the optimal parameter $p = \tilde{p}$ in a given domain that minimizes χ^2, Equation (14), which may be reformulated in the notation of this appendix as follows,

$$\chi^2(p) = \sum_{i=1}^{N} \delta f_i^{-2}[f_i - V_i(p)]^2, \tag{B1}$$

where δf_i^2 is the variance associated with the data f_i. By expanding $\chi^2(p)$ over its local minimum value, we obtain the following positive-definite quadratic form:

$$\chi^2(p) = A_0 + A_2(p-\tilde{p})^2 + O[(p-\tilde{p})^3], \tag{B2}$$

where $A_0 \geqslant 0$. $A_0 = 0$ corresponds to the optimal fit and $A_2 > 0$ represents the curvature of the fit. These coefficients (A_0, A_2) are analytically given by Livadiotis (2007),

$$A_0 = \chi^2(\tilde{p}) \tag{B3}$$

$$A_2 = \sum_{i=1}^{N} \delta f_i^{-2} \left\{ [V_i(\tilde{p}) - f_i] \frac{\partial^2 V_i(\tilde{p})}{\partial p^2} + \left[\frac{\partial V_i(\tilde{p}}{\partial p} \right]^2 \right\}. \tag{B4}$$

The uncertainty may be solved by minimizing the quantity $|p - \tilde{p}| = \sqrt{[\chi^2(p) - \chi^2(\tilde{p})]/A_2}$, which yields

$$\delta \tilde{p} = \sqrt{A_0/(MA_2)}, \tag{B5}$$

where M is the number of free parameters in the fit.

In the case that the χ^2 minimum is outside the domain, the χ^2 takes on the following positive-definite linear form:

$$\chi^2(p) = A_0 + A_1(p - \tilde{p}) + O[(p - \tilde{p})^2], \tag{B6}$$

where

$$A_1 = \sum_{i=1}^{N} \delta f_i^{-2} [V_i(\tilde{p}) - f_i] \frac{\partial V_i(\tilde{p})}{\partial p}. \tag{B7}$$

Minimization of the deviation, $|p - \tilde{p}|$, yields

$$\delta \tilde{p} = A_0/(M|A_1|). \tag{B8}$$

The formulae above are constructed based on perturbations of one parameter only. The multi-parameter generalization involves treatment of the terms p and $\tilde{p}$ as vectors. The generalization of Equations (B5) and (B8) is

$$\delta \tilde{p}_l = \sqrt{A_0 \left(A_2^{-1}\right)_{ll}/M} \sim \sqrt{A_0/(MA_{2,ll})} \tag{B9}$$

if the parameter $\tilde{p}_l$ is determined at a local χ^2 minimum. $A_{2,ll}$ is the principal curvature of the curve where only p_l varies, at the point $p_l = \tilde{p}_l$. Similarly,

$$\delta \tilde{p}_l = A_0/(M|A_{1,l}|), \tag{B10}$$

if the parameter is minimized at the boundary of the domain. In this case, $A_{1,l}$ is the slope of the χ^2 curve where only p_l varies, at the point $p_l = \tilde{p}_l$.

APPENDIX C

STATISTICS OF THE MEAN

While standard, we provide here for completeness the formulae for statistics of the mean used to construct Table 3. For a given set $\{x_i \pm \sigma_i\}_{i=1}^N$, the mean is weighted by the inverse variance,

$$\bar{x} = \left(\sum_{i=1}^{N} \sigma_i^{-2} \right)^{-1} \sum_{i=1}^{N} \sigma_i^{-2} x_i. \tag{C1}$$

The standard deviation through uncertainty propagation is

$$\sigma_{\rm prop} = \sqrt{\left(\sum_{i=1}^{N} \sigma_i^{-2} \right)^{-1}}. \tag{C2}$$

There is a second uncertainty associated with the statistical fit given by

$$\sigma_{\rm stat} = \sqrt{\frac{1}{\tilde{N} - 1} \left[\left(\sum_{i=1}^{N} \sigma_i^{-2} \right)^{-1} \sum_{i=1}^{N} \sigma_i^{-2} (x_i - \bar{x})^2 \right]}, \tag{C3}$$

where

$$\tilde{N} = N + 1 - N \left(\sum_{i=1}^{N} \sigma_i^{-2} \right)^{-2} \sum_{i=1}^{N} \sigma_i^{-4} \approx N. \tag{C4}$$

The total uncertainty is the root sum square of the propagation and statistical uncertainties,

$$\sigma_{\rm total} = \sqrt{\sigma_{\rm stat}^2 + \sigma_{\rm prop}^2}. \tag{C5}$$

REFERENCES

Artzner, G., Vial, J. C., Lemaire, P., Gouttebroze, P., & Leibacher, J. 1978, ApJL, 224, L83
Baranov, V. B., & Malama, Y. G. 1993, JGR, 98, 15157
Bonnet, R. M., Lemaire, P., Vial, J. C., et al. 1978, ApJ, 221, 1032
Bzowski, M., Kubiak, M. A., Möbius, E., et al. 2012, ApJS, 198, 12
Bzowski, M., Möbius, E., Tarnopolski, S., Izmodenov, V., & Gloeckler, G. 2008, A&A, 491, 7
Bzowski, M., Möbius, E., Tarnopolski, S., Izmodenov, V., & Gloeckler, G. 2009, SSRv, 143, 177
Bzowski, M., Sokol, J. M., Tokumaru, M., et al. 2011, arXiv:1112.2967
Bzowski, M., Sokół, J. M., Tokumaru, M., et al. 2013, Solar Parameters for Modeling the Interplanetary Background (ISSI Scientific Report Series, Vol. 13; New York: Springer Science and Business Media), 67
Chabrillat, S., & Kockarts, G. 1997, GeoRL, 24, 2659
Costa, J., Lallement, R., Quémerais, E., et al. 1999, A&A, 349, 660
Fahr, H. J. 1979, A&A, 77, 101
Funsten, H. O., Allegrini, F., Bochsler, P., et al. 2009, SSRv, 146, 75
Fuselier, S. A., Bochsler, P., Chornay, D., et al. 2009, SSRv, 146, 117
Holzer, T. E. 1977, RvGeo, 15, 467
Izmodenov, V., Malama, Y. G., Gloeckler, G., & Geiss, J. 2003, ApJL, 594, L59
Lallement, R., Quémerais, E., Bertaux, J. L., et al. 2005, Sci, 307, 1447
Lallement, R., Quémerais, E., Koutroumpa, D., et al. 2010, in AIP Conf. Proc. 1216, Twelfth International Solar Wind Conference, ed. M. Maksimovic, K. Issautier, N. Meyer-Vernet, M. Moncuquet, & F. Pantellini (Melville, NY: AIP), 555
Lee, M. A., Kucharek, H., Möbius, E., et al. 2012, ApJS, 198, 10
Lemaire, P., Charra, J., Jouchoux, A., et al. 1978, ApJL, 223, L55
Lemaire, P., Emerich, C., Curdt, W., Schühle, U., Wilhelm, K., et al. 1998, A&A, 334, 1095
Lemaire, P., Emerich, C., Vial, J.-C., et al. 2002, in From Solar Min to Max: Half a Solar Cycle with SOHO, ed. A. Wilson (ESA Special Publication, Vol. 508; Noordwijk: ESA), 219
Lemaire, P., Emerich, C., Vial, J.-C., et al. 2005, AdSpR, 35, 384
Linsky, J. L., & Wood, B. E. 1996, ApJ, 463, 254
Livadiotis, G. 2007, PhyA, 375, 518
Marquardt, D. W. 1963, J. Soc. Ind. Appl. Math., 11, 431
McComas, D. J. 2012, ApJS, 198, 8
McComas, D. J., Alexashov, D., Bzowski, M., et al. 2012, Sci, 336, 1291
McComas, D. J., Allegrini, F., Bochsler, P., et al. 2009, SSRv, 146, 11
Möbius, E. 2009, SSRv, 143, 465
Möbius, E., Bochsler, P., Bzowski, M., et al. 2012, ApJS, 198, 11
Möbius, E., Bzowski, M., Chalov, S., et al. 2004, A&A, 426, 897
Press, W. H., Teukolsky, S. A., Vetterling, W. T., & Flannery, B. P. 1992, Numerical Recipes in C (2nd ed.; Cambridge: Cambridge Univ. Press)

Quémerais, E., Bertaux, J.-L., Lallement, R., et al. 1999, JGR, 104, 12585
Saul, L., Wurz, P., Rodriguez, D., et al. 2012, ApJS, 198, 14
Scherer, H., Fahr, H. J., Bzowski, M., & Ruciński, D. 2000, A&AS, 274, 133
Schwadron, N. A., Crew, G., Vanderspek, R., et al. 2009, SSRv, 146, 207
Tarnopolski, S., & Bzowski, M. 2009, A&A, 493, 207
Vidal-Madjar, A. 1975, SoPh, 40, 69
Wallis, M. K. 1975, Natur, 254, 202
Warren, H. P., Mariska, J. T., & Wilhelm, K. 1998, ApJS, 119, 105
Witte, M., Banaszkiewicz, M., Rosenbauer, H., & McMullin, D. 2004, AdSpR, 34, 61
Witte, M., Rosenbauer, H., Banaszkiewicz, M., & Fahr, H. 1993, AdSpR, 13, 121
Wood, B. E., Izmodenov, V. V., Linsky, J. L., & Alexashov, D. 2007a, ApJ, 659, 1784
Wood, B. E., Izmodenov, V. V., Linsky, J. L., & Malama, Y. G. 2007b, ApJ, 657, 609
Woods, T. N., Rottman, G. J., White, O. R., Fontenla, J., & Avrett, E. H. 1995, ApJ, 442, 898
Zieger, B., Opher, M., Schwadron, N. A., McComas, D. J., & Toth, G. 2013, GeoRL, 40, 2923